Available online at www.sciencedirect.com
SCIENCE DIRECT®
International Journal of Heat and Fluid Flow 26 (2005) 349–361
International Journal of HEAT AND FLUID FLOW
www.elsevier.com/locate/ijhff

Flow analyses in a high-pressure axial ventilation fan with a non-linear eddy-viscosity closure

Alessandro Corsini *, Franco Rispoli

Dipartimento di Meccanica e Aeronautica, University of Rome "La Sapienza", Via Eudossiana, 18, Roma 00184, Italy

Received 26 October 2003; accepted 5 October 2004
Available online 23 November 2004

Abstract

A computational study is presented which investigates the predictive performance of a non-linear turbulence closure in simulating the flow physics pertinent to a high-pressure axial ventilation fan. The studied employed a cubic k–ε model which is considered as a promising closure for improving the state-of-the-art of industrial CFD by accounting for non-equilibrium effects.

The axial fan studied represents a challenge for simulation because of the presence of large three-dimensional interblade flow structures and strong leakage effects. The potential improvement of non-isotropic closures has been assessed with respect to a classical linear k–ε model. The comparative analyses aimed at the prediction of flow structure within the blades and close to the rotor tip clearance. The rotor design point and near-pressure-peak operating conditions have been simulated. The non-linear model is shown to provide a better base-line for non-equilibrium effects simulation with respect to the standard one. The authors adopt a parallel multi-grid algorithm developed for a highly accurate Petrov–Galerkin finite element method, here applied on equal-order Q1–Q1 as well as mixed Q2–Q1 element pairs. The parallel solution algorithm for Reynolds Averaged Navier–Stokes modelling exploits an overlapping domain decomposition technique based on an "inexact explicit non-linear Schwarz method".

1. Introduction

Computational fluid dynamics (CFD) when implemented with specific turbomachinery models and carefully planned experimental campaigns (e.g. Furukawa et al., 1998; Gallimore et al., 2002a), has been shown to be an effective investigation tool to enhance the understanding of flow features found in turbomachinery. With respect to decelerating axial turbomachinery, several CFD based research programs have been carried out to tackle the detection of complex aerodynamical effects. To mention but a fews we note the studies related to non-conventional blade design concepts (Wennerstrom, 1984; Rabe et al., 1957; Hah and Wennerstrom, 1991; Copenhaver et al., 1996; Wadia et al., 1997; Corsini and Rispoli, 2003), or to the tip leakage flows (Hah, 1986; Storer and Cumpsty, 1991; Goyal and Dawes, 1993; Lee et al., 1996; Furukawa et al., 1998; Corsini and Rispoli, 1999).

In turbomachinery flows non-equilibrium phenomena can not be resolved adequately with the Boussinesq effective viscosity concept. The overview of recent open literature on computational studies for compressors, indicates that the turbulence models in use range from simple algebraic eddy-viscosity models (EVMs) (e.g. Kang and Hirsch, 1996; Chima, 1998; Furukawa et al., 1999; Gallimore et al., 2002b), to one-equation Spalart–Almaras (Eulitz, 2001) or isotropic two-equation models with low-Reynolds number extensions (Hah and Loellbach, 1999; Van Zante et al., 2000). More advanced models, such as non-equilibrium eddy-viscosity variants (Chen et al., 1998; Borello et al., 1997), are occasionally adopted. Only recently, have appeared second moment closure applications to two- and

* Corresponding author. Tel.: +39 06 445 85 231; fax: +39 06 448 17 59.
E-mail address: corsini@dma.ing.uniromal.it (A. Corsini).

0142-727X/$ - see front matter © 2004 Elsevier Inc. All rights reserved.
doi:10.1016/j.ijheatfluidflow.2004.10.002

Nomenclature

B	force vector
C_p	pressure coefficient
D	isotropic dissipation rate at the wall
e_{ijk}	permutation tensor
F_a, F_d	advective and diffusive fluxes
H	shape factor, $H = \delta^*/\theta^*$
K_B	blockage factor, $K_B = (r_c - \delta^*_{ac})^2 - (r_h + \delta^*_{ah})^2/(r_c^2 - r_h^2)$
k, k^+	dimensional and normalized turbulent kinetic energy
l_c	blade chord
l_ε	turbulent length scale
l.e.	blade leading edge
Ma	Mach number
nsd	number of space dimension
P_k	turbulence energy production rate
p	static pressure
Re	Reynolds number
R	dimensionless radius, $R = r/R_c$
r	radius
S_{ij}, S	strain tensor and invariant
TI	turbulence intensity
t	time abscissa
t.e.	blade trailing edge
u_i	Cartesian velocity component
$\bar{u}, \bar{u}^+$	dimensional and normalized streamwise velocity
u_c	relative peripheral velocity at the casing
u_τ	friction velocity
$\overline{u_i' u_j'}$	Reynolds stress tensor
W_{ij},W	vorticity tensor and invariant
x, y, z	Cartesian coordinates
y_n^+	normalized distance to the wall, $(y_n^+ = u_\tau y_n/\nu)$

Greeks

δ^*	displacement thickness, $\delta^*_a = \int_0^{\delta_e} (1 - \bar{u}_a/\bar{u}^e_a)\,dn$
δ_{ij}	Kronecker delta
ε	dissipation rate of k
$\tilde{\varepsilon}$	homogeneous dissipation rate of k,$\tilde{\varepsilon} = \varepsilon - D$
θ^*	momentum thickness, $\theta^*_a = \int_0^{\delta_e} (1 - \bar{u}_a/\bar{u}^e_a)(\bar{u}_a/\bar{u}^e_a)\,dn$
ν	kinematic viscosity
ρ	fluid density
τ	turbulence time scale
φ_a	axial flow coefficient, $(\varphi_a = \bar{u}_a/u_c)$
φ_r	radial flow coefficient, $(\varphi_r = \bar{u}_r/uc)$
ψ	swirl flow coefficient, $(\psi = 2R(\bar{u}_p/u_c))$
Ω	computational domain
ω	frame angular velocity

Superscripts and subscripts

I	node adjacent to the wall
$'$	fluctuating quantity
$\bar{}$	averaged quantity
a, p, r	axial, peripheral and radial components
c	casing
D	Dirichlet value, or design condition
e	boundary layer edge
h	hub
i,j,k,l,m	Cartesian components
in	inlet value
N	Neumann value
n	normal direction
t	turbulent quantity

three-dimensional (3D) compressor cascade flows (Chen and Leschziner, 1999; Gerolymos et al., 2002). This state of the art is mainly related to the need to work with so-called engineering turbulence approaches giving ease of coding and numerical robustness, that has constrained industrial research to algebraic (Gallimore et al., 2002b) or standard two-equation EVMs. As a result remains an unsatisfactory level of accuracy in demanding flow problems, and the reliability of numerical simulations can not be guaranteed.

From the modelling viewpoint, in this paper the proposed methodology adopts a non-linear k–ε model (Craft et al., 1996), considered as a fair baseline in turbomachinery simulation, as it includes provisions to account for curvature and non-equilibrium effects, and to reduce stagnation-point problems. This turbulence closure, still undergoing validation efforts in several flow problems (such as: external aerodynamics, environmental problems, etc.), has not yet been extensively applied in the context of real turbomachinery configurations. Exceptions include work carried out by Chen et al. (1998) and the validation studies carried out at our Department on hydraulic turbines (Borello et al., 1997), and compressor cascade flows (Corsini and Rispoli, 2002).

From a numerical viewpoint, the authors adopt a parallel multi-grid (MG) method developed for the in-house made FEM code (Borello et al., 2001). The FEM formulation is based on a highly accurate stabilized Petrov–Galerkin (PG) method modified for the application to 3D equal- and mixed-order spatial approximations (Borello et al., 2003).

The present contribution examines the predictive capabilities of the studied cubic two-equation model in simulating a high-pressure axial ventilation fan. The fan, designed with a non-free vortex concept (NFV), is

widely used in high specific performance turbomachine units, i.e. performing simultaneously high flow rate (e.g. in the range from 5 to 15 $m^{(3)}/s$) [1] and total pressure rise (e.g. in the range from 500 to 1000 Pa) [1] with moderate rotor diameter, blade number, and rotational speed. The spanwise change in blade circulation results in characteristic 3D blade-to-blade flow, manifesting itself as a torsion of interblade stream-surface segments. As pointed out by the concerted experimental and computational investigation of Corsini et al. (1999), the NFV design concept results in a 3D secondary flow filling the dominant part of the rotor blade passages, and causing a torsion of interblade stream-surface segments.

The characteristics of the studied two-equation non-isotropic closure are first systematically assessed including validation studies on a flat-plate with semi-circular leading edge, and a compressor cascade comprising double-circular-arc blades. Moreover the potential improvement of cubic model is evaluated in the prediction of NFV high-pressure axial fan rotor. The comparative analyses are focused on the flow structure within the blades, on the rotor clearance. The studied operating conditions include the rotor design point, a reduced flow rate condition close to the near-pressure-peak. Particular emphasis is given to the survey of rotor flow in off-design operating conditions where severe non-equilibrium phenomena develop.

2. Turbulence models

2.1. Two-equation modelling

While second-moment closure is widely seen as the optimum level for complex flows there is growing interest in the alternative simpler routes for approximating the Reynolds stresses. These methods are founded on the use of a non-linear algebraic connection between stress and strain, following the non-Newtonian fluids analogy suggested by Rivlin (1957). Such relationships may be arrived at by simplifying stress-transport models (so-called algebraic stress models) (Pope, 1975) or by tensor representations, generally routed on the invariant theory in continuum mechanics (Lumley, 1970), which are kinematic relations that mimic the functional dependences of stress anisotropies.

The model examined here, proposed by Craft et al. (1996) and labeled CLS96, is an expression of the latter approach. The non-isotropic constitutive relation is modeled in the form of a third-order polynomial of the mean strain and vorticity tensors, and scalar turbulent viscosity ν_t. As assessed by the validation studies here presented, the stress-strain cubic dependence is a means to establish an appropriate sensitivity to streamline curvature (Chen and Leschziner, 1999). By adopting the Reynolds averaging, the full tensor functional form is

$$\begin{aligned}\overline{u_i'u_j'} = {} & \frac{2}{3}k\delta_{ij} - \nu_t S_{ij} - 0.1\nu_t\frac{k}{\varepsilon}\left(S_{ik}S_{kj} - S_{kl}S_{kl}\frac{1}{3}\delta_{ij}\right) \\ & + 0.1\nu_t\frac{k}{\varepsilon}\left(W_{ik}S_{kj} + W_{jk}S_{ki}\right) + 0.26\nu_t \\ & \times\frac{k}{\varepsilon}\left(W_{ik}W_{kj} - W_{kl}W_{kl}\frac{1}{3}\delta_{ij}\right) \\ & - 10c_\mu^2\nu_t\left(\frac{k}{\varepsilon}\right)^2\left(S_{ki}W_{lj} + S_{kj}W_{li}\right)S_{kl} \\ & - 5c_\mu^2\nu_t\left(\frac{k}{\varepsilon}\right)^2 S_{ij}S_{kl}S_{kl} + 5c_\mu^2\nu_t\left(\frac{k}{\varepsilon}\right)^2 S_{ij}W_{kl}W_{kl} \end{aligned} \quad (1)$$

where $S_{ij} = \left(\bar{u}_{i,j} + \bar{u}_{j,i}\right)$ is twice the strain tensor, $W_{ij} = \left(\bar{u}_{i,j} - \bar{u}_{j,i}\right) + 2e_{mji}\omega_m$ is twice the absolute vorticity tensor, ω_m is the frame angular velocity, e_{mji} is the permutation tensor, and δ_{ij} is the Kronecker tensor.

The non-isotropic model under investigation is coupled with a two-equation closure. The turbulent velocity- and length-scales are determined by solving conservation equations for the turbulent kinetic energy (k) and the commonly used homogeneous turbulent dissipation rate ($\tilde{\varepsilon}$), that read as

$$\frac{Dk}{Dt} = -\overline{u_i'u_j'}\cdot\bar{u}_{i,j} - \tilde{\varepsilon} + [(\nu + \nu_t/\sigma_k)k_{,i}]_{,i} + D \quad (2)$$

$$\frac{D\tilde{\varepsilon}}{Dt} = -C_{\varepsilon 1}\frac{\tilde{\varepsilon}}{k}\overline{u_i'u_j'}\cdot\bar{u}_{i,j} - C_{\varepsilon 2}f_{\varepsilon 2}\tau\tilde{\varepsilon} + E + [(\nu + \nu_t/\sigma_\varepsilon)\tilde{\varepsilon}_{,i}] \quad (3)$$

where ν_t is defined as: $\nu_t = C_\mu f_\mu \tau k$, $\tau = k/\tilde{\varepsilon}$ and D is the isotropic dissipation rate at the wall $D = 2\nu(\partial\sqrt{k}/\partial x_i)^2$.

Table 1 shows the values of the scale-determining equation coefficients, including the non-linear set and the standard one first introduced by Launder and Sharma (1974) isotropic model, labeled LS74. In Table 1: $Re_t = k^2/\nu\tilde{\varepsilon}$ is the turbulence Reynolds number, S and W are, respectively, the strain and vorticity invariants defined as $S = \tau\sqrt{0.5S_{ij}S_{ij}}$ and $W = \tau\sqrt{0.5W_{ij}W_{ij}}$.

2.2. Problem statement

The dynamic response of incompressible turbulent fluids is modeled in a non-inertial Cartesian frame of reference. The boundary value problem is written for the following set of fluid quantities (momentum components $\rho\bar{u}_i$ $(i = 1, 2, 3)$ (where ρ is the density of the fluid assumed constant, and $\bar{u}_i$ the Cartesian velocity components), static pressure p, turbulent kinetic energy k, and the dissipation variable $\tilde{\varepsilon}$, in general form:

[1] The performance data refer to the following configurations: 1000 mm outer diameter, 960 rpm, 1.2 kg/m^3 air density (Corsini et al., 2004).

Table 1
Closure coefficients in k and ε equations

	Non-linear EVM, CLS96	Linear EVM, LS74
C_μ	$\frac{0.3[1-\exp[-0.36/\exp[-0.75\max(S,W)]]]}{1+0.35[\max(S,W)]^{1.5}}$	0.09
f_μ	$1-\exp[-(Re_t/90)^{0.5}-(Re_t/400)^2]$	$\exp(-3.4/(1+Re_t/50)^2$
$C_{\varepsilon 1}$	1.44	1.44
$C_{\varepsilon 2}$	1.92	1.92
$f_{\varepsilon 2}$	$[1-0.3\exp(-Re_t^2)]$	$[1-0.3\exp(-Re_t^2)]$
E	$0.0022Sk\tau\nu_t(\partial^2\bar{u}_i/\partial x_j\partial x_k)^2$	$2\nu\nu_t(\partial^2\bar{u}_i/\partial x_j\partial x_k)^2$
σ_ε	1.3	1.3
σ_k	1	1

$$\begin{aligned} &F_{\mathrm{a},j}+F_{\mathrm{d},j}+\rho B=0 && \text{in } \Omega, \text{ for } j=1,2,3\\ &\overline{U}=\varphi_D && \text{on } \partial\Omega_D\\ &F_{\mathrm{d},n}=\varphi_N && \text{on } \partial\Omega_N \end{aligned} \tag{4}$$

The boundary conditions, provided along the computational domain boundary $\partial\Omega=\partial\underline{\Omega}_N\cup\partial\underline{\Omega}_D$ ($\partial\underline{\Omega}_N$ and $\partial\underline{\Omega}_D$) are closed disjoint subsets of $\partial\Omega$), generally prescribe inflow Dirichlet conditions (φ_D) and outflow Neumann conditions (φ_N). On the solid boundaries non-slip conditions are used, with the dissipation variable set as the homogeneous counter-part of the ε i.e. $\varphi_{D\tilde{\varepsilon}}=0$.

$\overline{U}$ is the fluid averaged variable vector:

$$\overline{U}\equiv[\,\bar{u}_1,\quad \bar{u}_2,\quad \bar{u}_3,\quad 0,\quad k,\quad \tilde{\varepsilon}\,]^{\mathrm{T}} \tag{5}$$

F_{a}, F_{d} are the advective and the diffusive fluxes respectively, that read as

$$F_{\mathrm{a}}\equiv[\,\bar{u}_j\rho\bar{u}_1,\quad \bar{u}_j\rho\bar{u}_2,\quad \bar{u}_j\rho\bar{u}_3,\quad \bar{u}_j\rho,\quad \bar{u}_j\rho k,\quad \bar{u}_j\rho\tilde{\varepsilon}\,]^{\mathrm{T}} \tag{6a}$$

$$F_{\mathrm{d}}\equiv\big[\bar{\tau}_{1j},\quad \bar{\tau}_{2j},\quad \bar{\tau}_{3j},\quad 0,\quad -\rho(\nu+\nu_t/\sigma_k)k_{,j},\quad -\rho(\nu+\nu_t/\sigma_k)\tilde{\varepsilon}_{,j}\big]^{\mathrm{T}} \tag{6b}$$

The stress tensor appearing in (6b) includes the non-linear Newtonian like turbulent stress terms, affecting the molecular kinematic viscosity ν with a scalar effective viscosity, and the pressure corrected by the turbulent spherical tensor part. The source vector B is given by

$$B\equiv[P_{\mathrm{M}1},\quad P_{\mathrm{M}2},\quad P_{\mathrm{M}3},\quad 0,\quad -P_k+\tilde{\varepsilon}+D,\quad -C_{\varepsilon 1}P_k\tilde{\varepsilon}/k+C_{\varepsilon 2}f_{\varepsilon 2}\tilde{\varepsilon}^2/k+E\big]^{\mathrm{T}} \tag{7}$$

Here the momentum components $P_{\mathrm{M}i}$ account for the non-inertial terms and for the volume sources originating from the treatment of higher-order terms in the non-isotropic stress-strain constitutive relation (Borello et al., 1997).

3. Numerical method

For the present study, the Navier–Stokes equations are solved by an original parallel MG FEM scheme (Borello et al., 2001). A consistent stabilised PG scheme was developed and applied to control the instability origins that affect the advective-diffusive incompressible flow limits (Borello et al., 2003), and the reaction of momentum and turbulent scale determining equations. The latter are, respectively, related to the Coriolis acceleration or to the dissipation/destruction terms in the turbulent scale determining equations (Corsini et al., 2004). Two stable finite-element spaces are used: a mixed Q2–Q1 element with quadratic interpolation of the velocity–turbulent variables and linear approximation of the pressure, and equal-order linear Q1–Q1 element. The chosen finite-element space combinations eliminate the undesirable pressure-checkerboarding effects related to piecewise constant interpolations. Concerning the solution strategy a hybrid full linear MG accelerator, first proposed in Borello et al. (2001), was built-into the in-house overlapping parallel solver. The Krylov iterations in the smoothing/solving MG phases are parallelized using an original additive domain decomposition algorithm. The message passing operations were managed using the MPI libraries. In that way, the fully coupled solution of the sub-domain problem involves an efficient non-conventional use of Krylov sub-space methods, based on the Generalized Minimal Residual (GMRes) algorithm. The preconditioned GMRes(m), with the order m of Krylov space dimension set to 5 when used as smoother and to 50 for the core solver.

4. Validation studies

In this section, we report on the numerical performance of the cubic EVM in predicting flow behaviour pertinent to turbomachinery. The flow configurations presented concern a flat-plate with a semi-circular leading edge, and a compressor cascade with Double-Circular-Arc (DCA) blade profile. The first flow case is used to assess the studied closures in predicting the separation-induced transition on a flat-plate under uniform free-stream flow. The latter case is a severe challenge for CFD codes, due to the presence of large separation regions arising along the highly curved blade surfaces even at near-design conditions. In what follows the non-isotropic model is evaluated against the reference numerical solutions provided by the standard k–ε model proposed by Launder and Sharma (1974).

4.1. Flow on a flat-plate with semi-circular leading edge

The leading edge flow under investigation reproduces the experimental results coded as T3L test case, carried out in the framework of the ERCOFTAC Transition Special Interest Group. In particular the experimental studies provided by Palikaras et al. (2002) for the zero pressure gradient case are here considered. The Reynolds number, based on inlet velocity and leading

edge radius ($r = 5$ mm) is equal to 1660. At the inlet, the free stream turbulence intensity (TI) is set to 7%, and the dissipation length l_ε value is 18 mm in accordance with Palikaras et al. (2002). The flow is assumed two-dimensional with constant temperature and incompressible.

A 12,681 node block-structured (H–O) grid has been used, with Q2–Q1 interpolation spaces. In the vicinity of the wall (O-connected region) have been placed 21 nodes. Close to the plate, the mesh refinement placed the closest node a dimensionless distance y_n^+ of about 1.0. At the inlet section of the computational domain, the experimental free-stream uniform profile is used for the mean velocity ($\bar{u} = 5$ m/s). Uniform distributions are also imposed for the turbulent variables, computed on the basis of inflow turbulence intensity and l_ε.

No-slip conditions are then applied on the plate surface, and homogeneous Neumann conditions are imposed at the outlet section.

The boundary layer on the flat-plate is investigated in two axial locations, $x = 6$ mm and $x = 12$ mm. Fig. 1 presents the mean velocity streamwise development.

The comparison of computed profiles against measurements shows that CLS96 predicts well the boundary layer emerging from the stagnation point, and clearly outperforms the linear predictions. Moreover, in Fig. 2, the comparison of streamwise velocity fluctuation profiles confirms the improved simulating capabilities gained by the cubic model.

4.2. Double circular arc cascade flow

The second test case deals with a DCA compressor cascade, experimentally studied by Zierke and Deutsch (1989) using a one-component LDV system. The DCA blade profile has a 65° camber angle, a 20.5° stagger angle, a solidity of 2.14, and a chord length l_c of 228.6 mm.

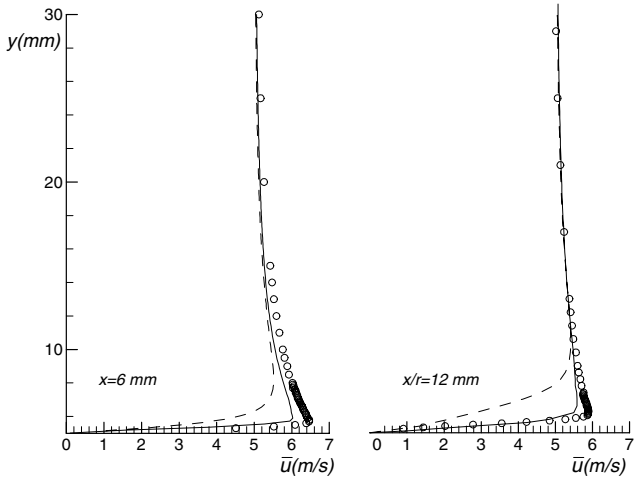

Fig. 1. T3L, streamwise mean velocity profiles at $x = 6$, 12 mm (symbols: experiments; dashed lines: LS74; solid lines: CLS96).

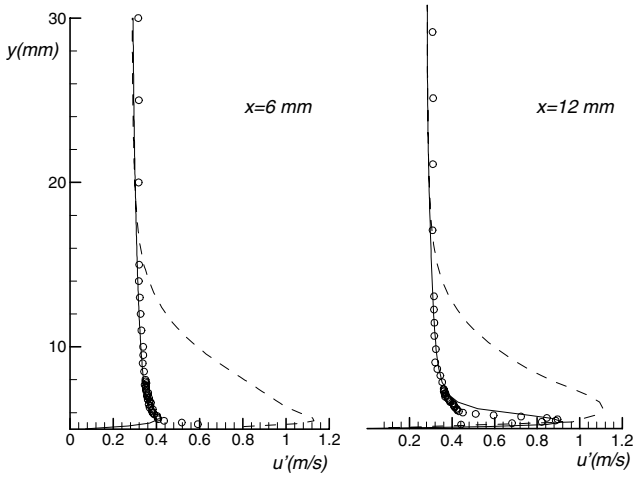

Fig. 2. T3L, streamwise velocity fluctuation profiles at $x = 6$, 12 mm (symbols: experiments; dashed lines: LS74; solid lines: CLS96).

The weak off-design condition with incidence angle −1.5° condition is here considered, which is highly challenging due to the presence of a separation-induced transition at the leading edge, followed by a larger separation in the rear portion of the blade. The chord Reynolds number, based on the inlet flow velocity $\bar{u}_{in}$, is set to 5.01×10^5. The flow is two-dimensional with constant temperature, and virtually incompressible ($Ma_{in} = 0.1$). A combined H–O topology was used to model the flow region, the mesh consists of 55274 nodes and is aligned with theoretical inlet and outlet flow directions. In the vicinity of the blade profile (O-connected region) 61 nodes are used to model the boundary layer normal to the blade surface on a quadratic interpolation basis. The grid refinement towards the blade surface sets the minimum dimensionless distance $y_n^+ = 0.1$. Inflow experimental free-stream values are used to set the Dirichlet conditions for mean velocity components, and turbulent variables (inflow TI = 2.0 %, and $l_\varepsilon/l_c = 2.0\%$).

The turbulence intensity contours around the blade leading edge are shown in Fig. 3.

The standard model prediction (Fig. 3a) is affected by an excessive TI level close to the stagnation region, that causes an anticipated transition. In contrast the CLS96 model, in Fig. 3b, is able to circumvent this anomaly, because of the sensitization of turbulence production and viscosity from the strain and vorticity tensors (Chen et al., 1998). As shown in Corsini and Rispoli (2002), the predicted turbulence level close to the stagnation point reaches a value of 1%, in agreement with earlier computations by Lien et al. (1998), with the use of Durbin's realizability constraint (Durbin, 1996).

Fig. 4 shows comparisons of velocity profiles on the blade suction side at 90.3% of the chord in the separation region, and on the pressure side at 20.5% of the chord where the boundary layer re-laminarizes. The boundary layer investigation in the suction side

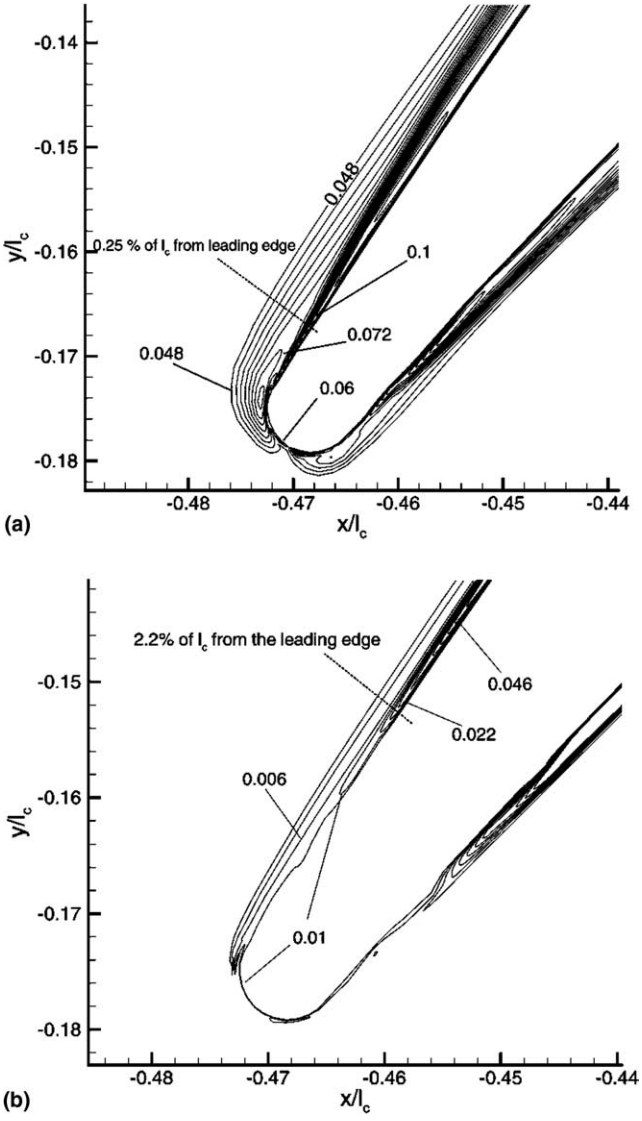

Fig. 3. Turbulence intensity contours near the leading edge: (a) model, and (b) CLS96 model.

separation region shows that the cubic CLS96 variant is the only able to return the separation, though an insufficient turbulent mixing leads to the under-estimation of the layer thickness. Moving in the front pressure side portion, it is remarkable that the non-linear model is able to resolve the re-laminarization of the fluid downstream the stagnation point in the presence of a mild adverse pressure gradient.

5. Rotor modelling and computed flow conditions

The axial ventilation fan has been designed for NFV operation and tested by Vad and Bencze (1998). The test rotor, labeled as BUP29, consists of 12 straight or unswept circular arc plate blades, with a hub-to-tip diameter ratio of 0.676, and an average tip clearance of

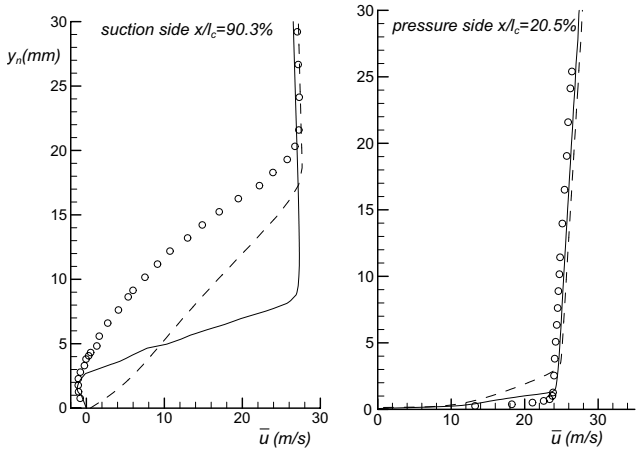

Fig. 4. DCA, streamwise mean velocity profiles on blade suction and pressure sides (symbols: experiments; dashed lines: LS74; solid lines: CLS96).

3 mm (relative height about 2% of mid-span chord). It was designed for a flow coefficient $\Phi_D = 0.5$ and a pressure rise coefficient $\Psi_D = 0.5$, prescribing a power function ideal total-head-rise distribution along the radius. The fan nominal rotational speed is 1100 rpm. Data on the airfoil geometry are provided in Fig. 5, together with a view of the rotor mesh. The thin blade profile permits one to extend the use of the H-grid topology to the modelling of the computational domain, which includes rotor blade passages and the clearance region, via the so-called "pinching" of the blade tip. The mesh consists of a non-orthogonal body-fitted coordinate system.

Three discretization levels have been used for the present calculations. The coarse mesh (C) has $59 \times 21 \times 31$ nodes (axial, pitch, spanwise), the mid mesh (M) $81 \times 31 \times 41$ nodes, and the fine mesh (F) $117 \times 41 \times 61$. The tested meshes share the node distributions in the axial direction, with the 20%, 50% and 30% of nodes respectively upstream the leading edge, in the blade passage and downstream of it. Moreover, there are 5 (C mesh), and 11 (M and F meshes) grid nodes to model the tip-clearance region. All the meshes have an adequate stretch towards the solid boundaries.

	BUP29 rotor		
	hub	midspan	tip
σ	1.53	1.24	1.05
γ, deg	47.9	42.2	38.3
θ, deg	27.4	23.1	19.9

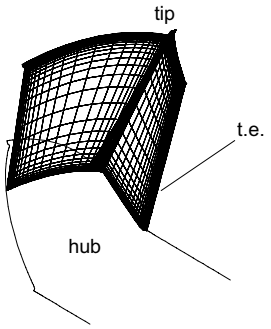

Fig. 5. BUP29 rotor, airfoil geometry and computational grid.

The adopted model for the wall boundary layers makes use of an analytical wall function with the conventional logarithmic velocity profile, modified for the turbomachinery CFD. The wall velocity profiles are computed in an intrinsic frame of reference defined on the boundary-layer edge surface.

In that way the peripheral velocity and stress components are directly affected by the relative casing motion, where u_c acts as non-zero limit in the integration of velocity profile across the layer. Ad-hoc techniques are used to circumvent the weaknesses of wall function in the presence of non-equilibrium flow features or, in general, non-shear dominated flows. In particular, we have used the friction velocity definition based on the turbulent kinetic energy, and a correction for its budget equation that assumes zero diffusion to the wall (Chieng and Launder, 1980).

The standard boundary conditions already used for the family of high performance fans under investigation are adopted (Corsini et al., 2001). Over the inflow section, 0.15 midspan chord upstream the hub leading edge, the Dirichlet conditions for the relative velocity components are obtained from the LDA upstream measurements (Vad and Bencze, 1998). The inlet distribution of k is obtained from an axi-symmetric turbulence intensity profile derived on the basis of the upstream LDA data, while the ε inlet profile was modeled with l_ε set as 1.0% of the rotor pitch at midspan. Flow periodicity is enforced by direct nodal coupling in the upstream and downstream regions and within the tip gap. The Neumann outflow conditions (homogeneous for k and ε and non-homogeneous for the static pressure) complete the set of boundary data.

The Reynolds number based on blade chord and blade peripheral velocity at mid-span was 3.5×10^5. Given that the performance of cubic model was to be investigated in the fan operational range, numerical studies have been carried out for the design point, $\Phi = \Phi_D = 0.5$, and a near-pressure-peak point, $\Phi = 0.4$.

6. Data analysis

Previous study using isotropic turbulence modelling indicate that the performance characteristics and rotor flow physics in the NFV axial fan family are well predicted (Corsini and Rispoli, 1999; Corsini et al., 2001). The effect of the mesh refinement is first discussed by comparing the integral properties of the casing wall boundary layer at rotor exit (0.047 chord downwind of the hub trailing edge). The following quantities have been considered: the axial displacement δ^*_a and momentum θ^*_a thicknesses, the shape H_a and blockage K_B factors. In Table 2 the values predicted with the tested meshes are compared to that measured by Vad and Bencze (1998). Data refer to the design operating condition,

Table 2
Boundary-layer integral parameters on the casing downstream of the rotor

	Measurements (Vad and Bencze, 1998)	Predictions (C)	Predictions (M)	Predictions (F)
δ^*_{a3} (mm)	2.7	3.29	2.91	2.79
θ^*_{a3} (mm)	2.1	2.29	1.97	2.07
H_{a3}	1.3	1.27	1.48	1.35
K_{B3}	0.95	0.92	0.921	0.937

and the numerical tests that have been carried out adopting the non-linear turbulence closure.

The computed boundary layer parameterization at the casing are in good agreement with experiments for all the tested discretizations, without achieving genuinely grid-independent results. Nevertheless, the finer level improves the prediction of the annulus boundary layer, in terms of velocity defect and energy content. From a design viewpoint, the analysis of flow integral properties also shows a slight underestimation of the computed blockage effect, that is markedly improved with the refinement of the mesh. The subsequent comparative flow survey is based on F-mesh numerical results.

6.1. Flow survey behind the rotor

The simulated rotor-flow physics resolved by linear and non-linear EVMs are compared by using the 3D flow structure behind the rotor. Relative to the design operating condition, Fig. 6 presents the computed and measured spanwise distributions of pitch-averaged axial $\bar{\varphi}_a$, radial $\bar{\varphi}_r$, and swirl flow coefficients $\bar{\psi}$. The LDA $\bar{\varphi}_a$ profile presents marked displacement zones close to the annulus walls. This basic tendency is generally reflected by the linear and non-linear predictions, though the computed velocity defect layers are overestimated.

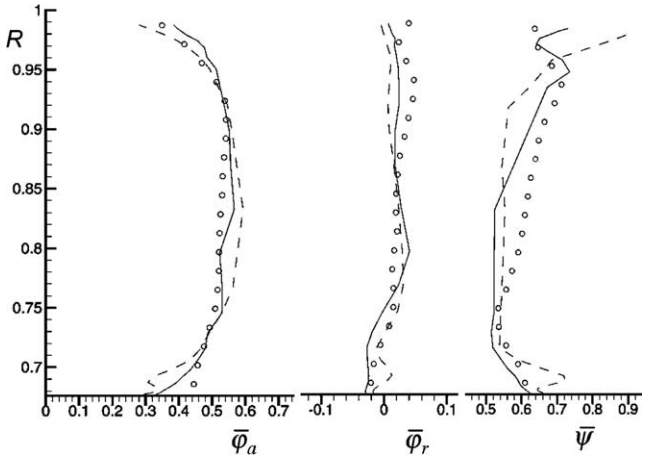

Fig. 6. Pitchwise-averaged flow data at rotor exit, $\Phi = 0.5$: axial flow coefficient; radial flow coefficient; swirl coefficient (symbols: experiments; dashed lines: LS74; solid lines: CLS96).

Nonetheless the blockage factor data show a clear improvement in the case of the non-isotropic model (e.g. the blockage factor K_B is 0.89 for the linear model, 0.937 for the non-linear one and 0.95 for the measurements).

Concerning the radial velocity $\bar{\varphi}_r$ profiles shown in Fig. 6, both the predicted distributions resolve the experimental profile only qualitatively. The non-linear model's radial velocity shows a good behaviour in the vicinity of the annulus walls, returning correctly the position of peak velocity near the blade tip while the positive peak below midspan is shifted outward.

With respect to $\bar{\psi}$ profiles, both the computations capture the slight overturning near the hub, due to the passage vortex effect on hub boundary layer. According to the spanwise increasing ideal total head rise, the measured outlet swirl increases with radius and it decreases near the casing due to the underturning effect of stationary wall and leakage flow.

This feature, essential for the validity of the numerical solution, is well resolved only by the non-linear model that is able to simulate the experimental swirl drop close to the blade tip.

The distribution of spanwise-velocity coefficients in near-peak pressure operation, shown in Fig. 7, gives further evidence of cubic closure improvements. For instance, the throttled axial velocity profiles show a fair agreement between measurements and non-linear prediction, accounting correctly for the velocity defect of the skewed annulus boundary layers. Furthermore, in the radial velocity plot the experimental net outward flow is captured by both the computations close to mid-span.

At larger radii the non-linear profile correctly predicts the peak radial velocity (i.e. about $R = 0.94$) but returns a mild defect layer. Finally, the comparison of swirl coefficient profiles confirms the capability of the cubic turbulence closure to account for the tip-leakage

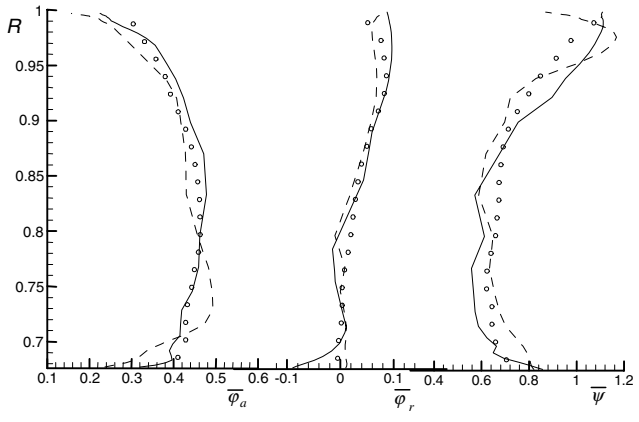

Fig. 7. Pitchwise-averaged flow data at rotor exit, $\Phi = 0.4$: axial flow coefficient; radial flow coefficient; swirl coefficient (symbols: experiments; dashed lines: LS74; solid lines: CLS96).

phenomena reproducing the marked attenuation of the leakage-driven underturning effect.

We complete this survey discussing the pitch-wise resolved flow structure. To this end, the local ideal total head rise or swirl coefficient ψ contours are compared at rotor exit for $\Phi = 0.5$ (Fig. 8) and $\Phi = 0.4$ (Fig. 9). The annular section is mapped onto its rectangular image with reference to radial and angular abscissae.

The computed distributions correctly predict the main flow features in the wake and the hub region. For example, the non-linear solution (Fig. 8c) shows a fair quantitative agreement with the LDA data in accounting for the swirl growth through the wake in the over-turning region close to the suction side corner.

Moving towards the tip, it is worth noting that both the predicted flow fields over-estimate the flow deviation at the higher radii. Notwithstanding it is encouraging that the non-linear model improves the standard prediction featuring a casing high-swirl core region, closer to the blade suction surface and a steeper annulus swirl defect. When the rotor is throttled to $\Phi = 0.4$, the LDA swirl map (Fig. 9a) shows an evident growth of swirl close to the casing through a wide annulus layer. This feature, related to an intense outward motion along the blade suction surface that is able to attenuate the leakage interaction, is well captured by the cubic solution (Fig. 9c) that establishes the physical swirl level at the blade tip. Moreover, approaching the hub suction side, the non-linear swirl map (Fig. 9c) clearly reproduces the swirl peak produced by the anti-clockwise secondary flow that washes the pitch from the pressure to the suction side.

6.2. Flow structure inside the blade passage

A meaningful presentation of flow developing within the blade passage is here built with reference to the fluid pattern near the rotor-blade suction surface, generally recognized as limiting the pressure rise and turning the blade profiles. The survey of 3D flow paths, induced by the design NFV concept and by the secondary-to-primary flow interaction, is given by the distributions of turbulence level in the vicinity of the blade leading edge and in the aft portion of the blade, at 10%, 65% and 98% midspan chord positions.

The suction surface survey is shown in Figs. 10 and 11 in terms of contours of static pressure coefficient C_p and limiting streamlines for the tested operating points. The rotor suction surface is plotted in a meridional view.

The analysis of suction side patterns at the design point (Fig. 10) returns as common flow features a corner stall-like pattern near the hub, and a clear outward motion. Despite these facts, the linear solution (Fig. 10a) shows a smaller reverse flow region which is not able to strengthen the flow centrifugal motion. The negative incidence at the hub, indicated by leading-edge suc-

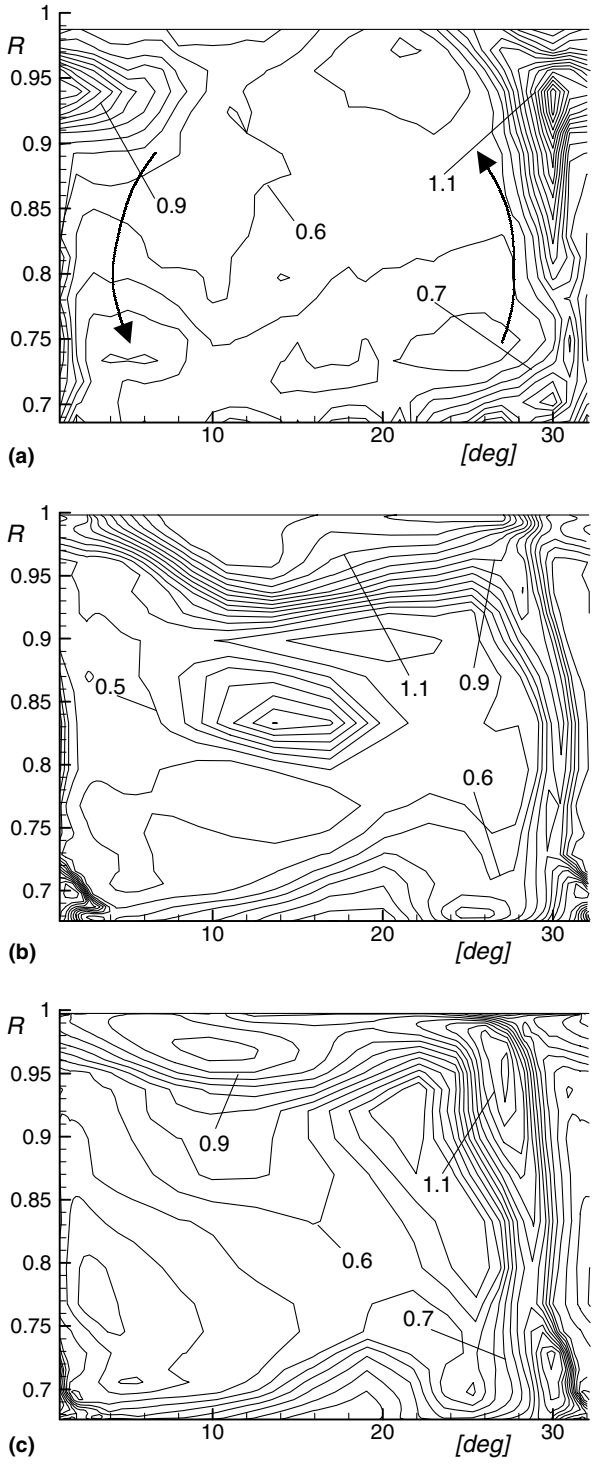

Fig. 8. Swirl coefficient ψ distributions at rotor exit, $\Phi = 0.5$: (a) experiments, (b) LS74; (c) CLS96.

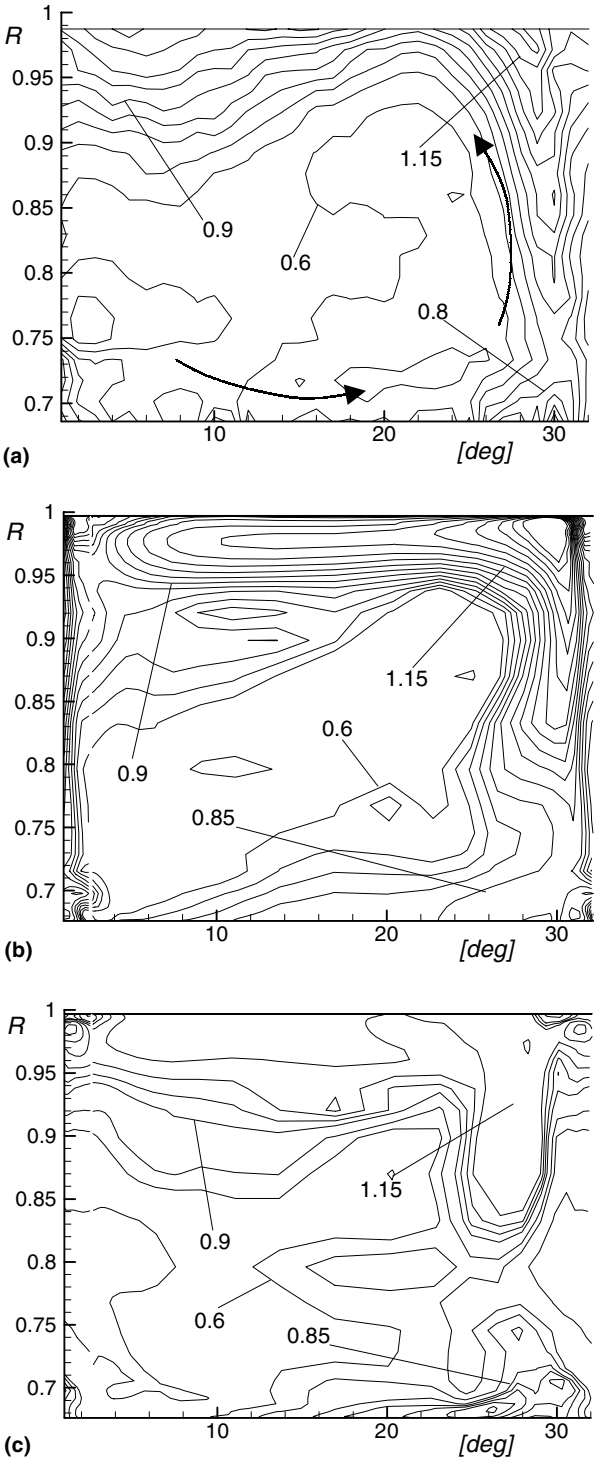

Fig. 9. Swirl coefficient ψ distributions at rotor exit, $\Phi = 0.4$: (a) experiments, (b) LS74; (c) CLS96.

tion-side pressure peaks, causes a steep acceleration up to 10% of chord. The related strain rate growth promotes high streamwise turbulence intensity and mixing giving the fluid the opportunity to resist the adverse pressure gradient effects. Looking at the non-linear solution (Fig. 10b), the evolution of the flow pattern along the chord is such that it results in a clear separation in the aft portion of the blade though the design operating condition.

Such a corner stall is basically the result of the cross-passage vortex that washes outward the suction surface, which is strengthened by the radial NFV induced flow.

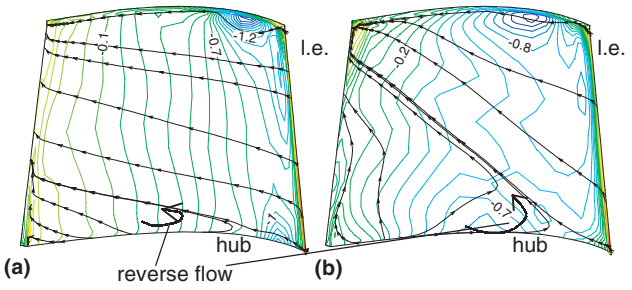

Fig. 10. Static pressure coefficient distribution and streamlines on the suction surface of the blade at $\Phi = 0.5$: (a) LS74 (b) CLS96.

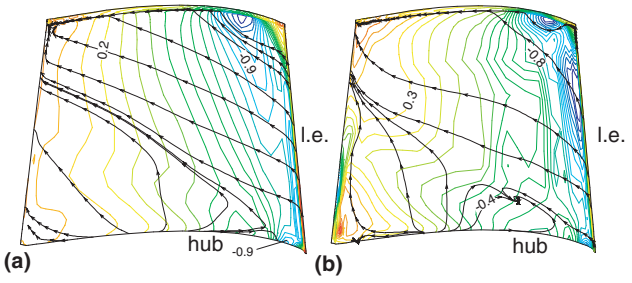

Fig. 11. Static pressure coefficient distribution and streamlines on the suction surface of the blade at $\Phi = 0.4$: (a) LS74, (b) CLS96.

In this simulation, a smoother favorable pressure gradient takes place after the leading edge incidence region, with attenuated turbulence level (i.e. $TI_{CLS96} = 0.12$ versus $TI_{LS74} = 0.2$). Moreover the fluid centrifuged from the separated region moves towards a re-attachment line with an outward meridional angle about 45°, revealed by isobar distortion with the appearance of typical pressure tough.

Concerning the blade tip aerodynamics, CLS96 predicts a leakage flow which emerges about 25% of chord clearly downwind with respect to the LS74 map. On the basis of the iso-bar comparison, it could be also inferred that the computed leakage flows develop along different trajectories. To this end, the cubic solution, in Fig. 10b, features a wider area of pressure distortion indicated by the leakage flow path being located closer to the blade suction-side.

When the rotor is throttled to the near-pressure peak condition, the increased incidence at the hub produces corner stall structures of greater complexity which are predicted by both linear and non-linear turbulence closures (Fig. 11). In this regard, CLS96 models a larger separation which develops from the front portion of the hub blade-section. Nevertheless the presence of the stalled section, up to 30% of the span, limits the outward inclination of the reattachment line thus preserving the loading capabilities of higher radii sections (Fig. 11b). Moving towards the tip, where the blade sections have the smallest stagger angles, the flow stems from the leading edge with a positive velocity spike. This is a consequence of the transfer of the stagnation point from the suction to the pressure surface, combined with the reduction of inlet flow rate through the annulus due to the operating point. In the non-linear computation (Fig. 11b) this circumstance produces a marked shifting upstream of leakage flow origin (i.e. whose chordwise position moves to the 14% of chord). The magnitude of isobar distortion, mainly concentrated about the suction-side origin, suggests also that the leakage flow develops through the vane with an increased angle of deviation to the axial direction. On the other hand, in the linear solution (Fig. 11a), the leakage-flow effects on the suction-side flow field appear to be less dependent from the operating point (i.e. the leakage flow origin is shifted upstream to 18% of the chord).

Finally the 3D chord-wise flow evolution is evidenced by turbulence level maps, at 10%, 65% and 98% of mid-span chord positions shown in Fig. 12.

This analysis is limited to the design operation where the rotor features distinct vortical structures associated to the leakage flow. Fig. 12 also describes the simulated leakage stream-paths.

The map of the chordwise evolution of turbulence level shows significant differences between the turbulence closures under investigation, mainly concentrated in the vicinity of the annulus end-walls (e.g. casing and hub).

Close to the suction side trailing edge at the hub (Fig. 12a), the LS74 map shows a turbulence peak related to the passage vortex structure, that is not present in the non-linear model due to the combined stress tensor sensitization to strain and vorticity (Fig. 12b). At the same section at higher radii, the linear model predicts the peak turbulence levels in the region where the leakage vortex develops. In this respect, the anisotropic solution features a tip leakage vortex that moves through a low turbulence energy core. The map at 65% chord (Fig. 12b) shows that the high turbulence core (e.g. peak value about 20%) on the casing, produced by the interaction between the centrifuged low energy fluid on the suction-side and the leakage flow, rapidly decays as the flow sheet rolls into the leakage vortical structure. This evidence, again, confirms that the cubic model (Fig. 12b) returns the physics of pure rotational flow correctly.

6.3. Flow structure inside the tip gap

In addition to the leakage stream-paths above commented, the behaviour of the flow within the rotor tip gap is also investigated in terms of static pressure isolines.

In particular is here considered a cylindrical surface with $R = 0.994$, placed at the 30% of the gap from the blade tip. The static pressure coefficient maps for the tested operating conditions are, respectively, shown in Figs. 13 and 14.

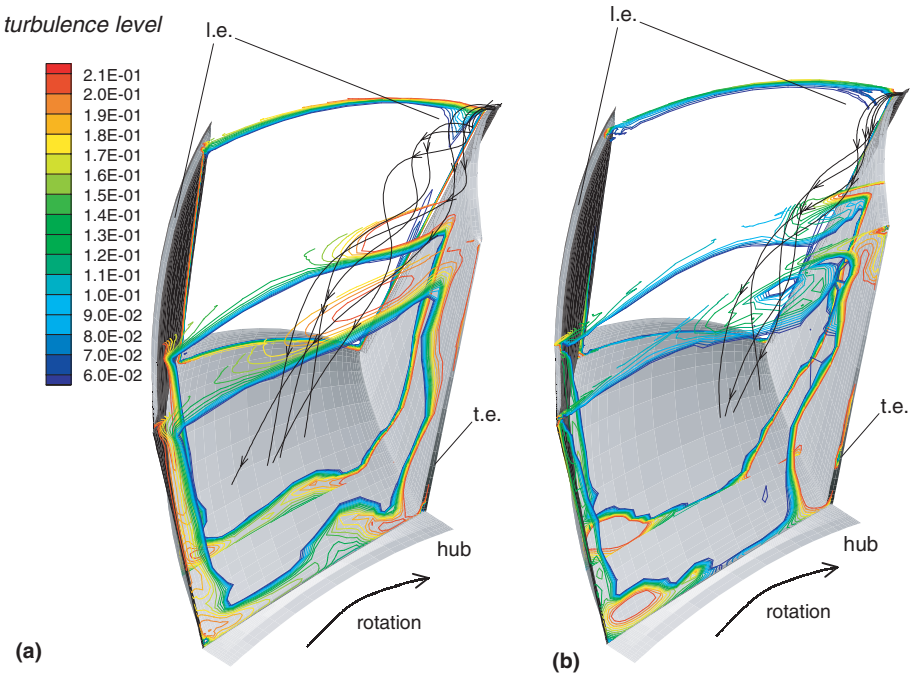

Fig. 12. Evolution of turbulence level and leakage streamlines inside the blade passage, in design operation: (a) LS74, (b) CLS96.

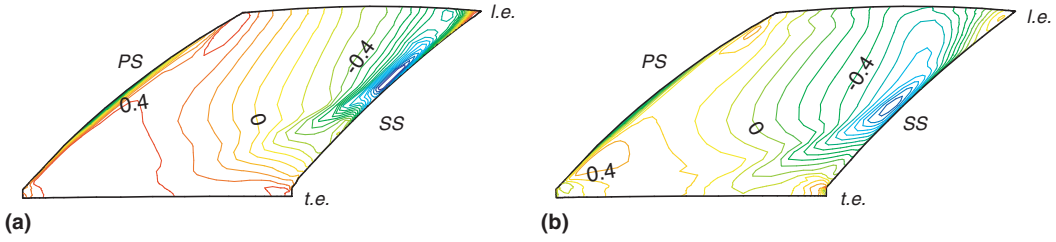

Fig. 13. Flow survey inside the tip gap at $R = 0.988$, design condition: (a) LS74 static pressure contour, (b) CLS96 static pressure contour.

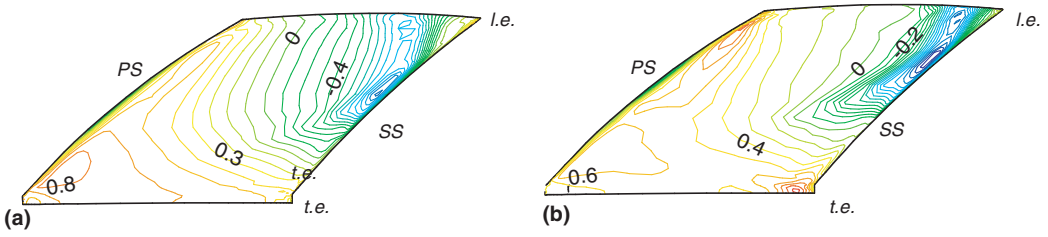

Fig. 14. Flow survey inside the tip gap at $R = 0.988$, near-peak pressure condition: (a) LS74 static pressure contour, (b) CLS96 static pressure contour.

In the design operating point, Fig. 13b, the CLS96 model features a leakage flow core which stems from suction side camber about the 20% to 25% of tip chord. The leakage flow is significantly fed also in the aft portion of the blade, with a maximum rate about 50% of the chord in clear agreement with the former experimental and numerical evidences provided by Storer and Cumpsty (1991) for a linear compressor cascade of similar relative gap. With respect to the LS74 solution (Fig. 13a), the CLS96 prediction features a leakage phenomenon of greater intensity which rolls into a vortical structure.

This is clearly indicated by the pressure troughs, tracing the vortex core on isobars in Fig. 13b, and by the leakage streamlines in Fig. 12b. Moreover, comparing the isobar maps in Fig. 13 it is noted that only the

CLS96 model is able to predict a leakage structure of sufficient strength to affect and under-turn the flow behind the rotor.

At the near-peak pressure point, Fig. 14, both models show reduced leakage flow effects. The global flow rate throttling results in a reduction of leakage flow rate and the leaked flow is not able to develop into a vortex. Nevertheless, the non-linear solution confirms its ability to predict a leakage flow of higher magnitude than the LS74 model, as shown by the isobar maps in Fig. 14.

7. Conclusions

The paper has investigated the performance of a cubic non-linear EVM when used to simulate a high-pressure axial ventilation fan. A FEM parallel MG method, developed by the authors, has been used with a higher-order approximation scheme in order to guarantee numerical accuracy on orthogonal and distorted quadrangular meshes.

The validation studies on circular leading-edge T3L flow and the DCA compressor cascade, confirmed the improvement obtained in the simulating capabilities by using the cubic turbulence closure in highly complex flow configurations pertinent to turbomachinery.

For the comparative analysis on the NFV axial ventilation fan, the non-linear model is shown to provide a better base-line for simulating non-equilibrium effects than the standard one. The following conclusions are drawn on the basis of the compared fluid dynamical behaviours, within the blade passage and close to the rotor tip clearance.

Concerning the flow survey behind the fan rotor for the tested operating points, the non-linear solution improves the swirl prediction reproducing the casing under- and over-turning, at design and throttled flow rates respectively in agreement with the available LDA data. This circumstance is related to the ability of the non-linear model to take account of the stall-like behaviour on the blade suction-side as well as the leakage phenomena. The sensitization of the cubic stress dependence to strain and vorticity is considered as critical to modelling accurately severe 3D flow structure which is not achievable with the linear eddy diffusivity approach.

Acknowledgments

The authors are indebted to Prof. B. Launder for the helpful comments and to Prof. J. Vad for providing rotor LDA data. The authors acknowledge MIUR support under the projects "Ateneo 2001" and "Facoltà 2002". The first author thanks also MIUR under the projects "Giovani Ricercatori".

References

Borello, D., Corsini, A., Rispoli, F., 1997. Prediction of Francis turbine runner performance using a 3D finite element technique with unassembled stiffness matrix treatment. In: 2nd European Conf. on Turbomachinery, Antwerp, Belgium.

Borello, D., Borrelli, P., Quagliata, E., Rispoli, F., 2001. A multi-grid additive and distributive parallel algorithm for finite element turbomachinery CFD. ECCOMAS-CFD 2001, Swansea, UK.

Borello, D., Corsini, A., Rispoli, F., 2003. A finite element overlapping scheme for turbomachinery flows on parallel platforms. Comput. Fluids 32 (7), 1017–1047.

Chen, W.L., Leschziner, M.A., 1999. Modeling turbomachine-blade flows with non-linear eddy-viscosity models and second moment closure. IMechE Paper C557/131/99, A, pp. 189–199.

Chen, W.L., Lien, F.S., Leschziner, M.A., 1998. Computational prediction of flow around highly loaded compressor—cascade blades with non-linear eddy-viscosity models. Int. J. Heat Fluid Flow 19, 307–319.

Chieng, C.C., Launder, B.E., 1980. On the calculation of turbulent heat transport downstream from an abrupt pipe expansion. Numer. Heat Transfer 3, 189–207.

Chima, R.V., 1998. Calculation of tip clearance effects in a transonic compressor rotor. J. Turbomach. 120, 131–140.

Copenhaver, W.W., Mayhew, E.R., Hah, C., Wadia, A.R., 1996. The effect of tip clearance on a swept transonic compressor rotor. J. Turbomach. 118, 230–239.

Corsini, A., Rispoli, F., 1999. Numerical simulation of three-dimensional viscous flow in an isolated axial rotor. Arch. Mech. Eng. XLVI-4, 369–392.

Corsini, A., Rispoli, F., 2002. Anisotropic turbulence modeling of near wall effects pertinent to turbomachinery flows. ASME Paper FEDSM02-31206.

Corsini, A., Rispoli, F., 2003. The role of forward sweep in subsonic axial fan rotor aerodynamics at design and off-design operating conditions. ASME Paper GT2003-38671.

Corsini, A., Rispoli, F., Bencze, F., Vad, J., 1999. Concerted experimental and numerical studies on axial flow fan rotor aerodynamics. IMechE Paper C557/106/99, B, pp. 519–531.

Corsini, A., Rispoli, F., Bencze, F., Vad, J., 2001. Effects of blade sweep in a high performance axial flow rotor. ATI-CST Paper 005/01, 4th European Conf. on Turbomachinery, Firenze, Italy.

Corsini, A., Rispoli, F., Santoriello, A., 2004. A new stabilized finite element method for advection-diffusion-reaction equations using quadratic elements. In: Lajos, T., et al. (Eds.), Modelling Fluid Flow. Springer-Verlag.

Craft, T.J., Launder, B.E., Suga, K., 1996. Development and application of a cubic eddy-viscosity model of turbulence. Int. J. Heat Fluid Flow 17, 108–155.

Durbin, P.A., 1996. On the k–ε stagnation point anomaly. Int. J. Heat Fluid Flow 17, 89–90.

Eulitz, F., 2001. Numerical simulation and modeling of unsteady turbomachinery flows. In: Recent Developments in Numerical Methods for Turbomachinery Flows. VKI LS 2002-2001.

Furukawa, M., Saiki, K., Nagayoshi, K., Kuroumaru, M., Inoue, M., 1998. Effects of stream surface inclination on tip leakage flow fields in compressor rotor. J. Turbomach. 120, 683–694.

Furukawa, M., Inoue, M., Saiki, K., Yamada, K., 1999. The role of tip leakage vortex breakdown in compressor rotor aerodynamics. J. Turbomach. 121, 469–480.

Gallimore, S.J., Bolger, J.J., Cumpsty, N.A., Taylor, M.J., Wright, P.I., Place, J.M.M., 2002a. The use of sweep and dihedral in multistage axial flow compressor blading. Part II: low and high-speed designs and test verification. J. Turbomach. 124, 533–541.

Gallimore, S.J., Bolger, J.J., Cumpsty, N.A., Taylor, M.J., Wright, P.I., Place, J.M.M., 2002b. The use of sweep and dihedral in

multistage axial flow compressor blading. Part I: University research and methods development. J. Turbomach. 124, 521–532.
Gerolymos, G.A., Neubauer, J., Sharma, V.C., Vallet, I., 2002. Improved prediction of turbomachinery flows using near-wall Reynolds-stress model. J. Turbomach. 121, 86–99.
Goyal, R.K., Dawes, W.N., 1993. A comparison of the measured and predicted flow field in a modern by-pass configuration. J. Turbomach. 115, 273–282.
Hah, C., 1986. A numerical modeling of endwall and tip-clearance flow of an isolated compressor rotor. J. Eng. Power 108, 15–21.
Hah, C., Loellbach, J., 1999. Development of hub corner stall and its influence on the performance of axial compressor blade rows. J. Turbomach. 121, 67–77.
Hah, C., Wennerstrom, A.J., 1991. Three-dimensional flowfields inside a transonic compressor with swept blades. J. Turbomach. 113, 241–251.
Kang, S., Hirsch, C., 1996. Numerical simulation of three-dimensional viscous flow in a linear compressor cascade with tip clearance. J. Turbomach. 118, 492–505.
Launder, B.E., Sharma, B.I., 1974. Application to the energy-dissipation model of turbulence to the calculation of flow near a spinning disc. Int. J. Heat Mass Transfer 1, 131–138.
Lee, Y.T., Hah, C., Loellbach, J., 1996. Flow analyses in a single-stage propulsion pump. J. Turbomach. 118, 240–249.
Lien, F.S., Kalitzin, G., Durbin, P.A., 1998. RANS modeling for compressible and transitional flows. In: Proceed. of Summer Program—Center for Turbulence Research, pp. 267–286.
Lumley, J.L., 1970. Toward a turbulent constitutive relation. J. Fluid Mech. 41, 413–434.
Palikaras, A., Yakinthos, K., Goulas, A., 2002. Transition on a flat plate with a semi-circular leading edge under uniform and positive shear free-stream flow. Int. J. Heat Fluid Flow 23, 421–430.
Pope, S.B., 1975. A more general effective-viscosity hypothesis. J. Fluid Mech. 72, 331–340.
Rabe, D., Hoying, D., Koff, S., 1991. Application of sweep to improve efficiency of a transonic fan: Part II. Performance and laser test results, AIAA paper 91-2544.
Rivlin, R.S., 1957. The relation between the flow of non-Newtonian fluids and turbulent Newtonian fluids. Quart. Appl. Math. 15, 212–215.
Storer, J.A., Cumpsty, N.A., 1991. Tip leakage flow in axial compressors. J. Turbomach. 113, 252–259.
Vad, J., Bencze, F., 1998. Three-dimensional flow in axial flow fans of non-free vortex design. Int. J. Heat Fluid Flow 19, 601–607.
Van Zante, D.E., Strazisar, A.J., Wood, J.R., Hathaway, M.D., Okiishi, T.H., 2000. Recommendations for achieving accurate numerical simulation of tip clearance flows in transonic compressor rotors. J. Turbomach. 122, 733–742.
Wadia, A.R., Szucs, P.N., Crall, D.W., 1997. Inner working of aerodynamic sweep. ASME Paper 97-GT-401.
Wennerstrom, A.J., 1984. Experimental study of a high-through-flow transonic axial compressor stage. J. Gas Turbine Power 106, 552–560.
Zierke, W.C., Deutsch, S., 1989. The measurement of boundary layers on a compressor blade in cascade, vol. 2. Data Tables and Final Report. NASA-CR-185118.